Parity-time-symmetry-enabled broadband quantum frequency-comb generation

Nuo Chen,[1] Wuqiang Chi,[1] Yunru Fan,[2] Hanghang Li,[1] Zijie Wang,[1] Qiang Zhou,[2,3,*] Jing Xu,[1,4,†] and Xinliang Zhang[4,‡]
[1]*School of Optical and Electronic Information, Huazhong University of Science and Technology, Wuhan 430074, China*
[2]*Institute of Fundamental and Frontier Sciences, University of Electronic Science and Technology of China, Chengdu 610054, China*
[3]*Center for Quantum Internet, Tianfu Jiangxi Laboratory, Chengdu 641419, China*
[4]*Wuhan National Laboratory for Optoelectronics, Huazhong University of Science and Technology, Wuhan 430074, China and Optics Valley Laboratory, Hubei 430074, China*

(Received 7 May 2024; accepted 30 July 2024; published 13 August 2024)

Microcavities stand out as competitive tools in the development of quantum frequency combs (QFCs) for multiphoton entanglement sources, frequency-multiplexed single-photon sources, and the generation of high-dimensional entangled states. However, the presence of waveguide dispersion hinders the creation of broadband QFCs, an issue that becomes increasingly critical as the quality factor of the microcavity increases. Here, we present a scheme to enhance the spectral range of QFCs by selectively manipulating the pump resonance via parity-time symmetry. We show that by using pulsed pump light to cover the pump resonance, frequency-matching conditions can be relaxed and the spectral range of QFCs can thus be significantly extended near the exceptional point. The proposed method offers a simple, effective, and robust approach to increase the dimension of QFCs, without severely sacrificing nonlinear efficiency.

DOI: 10.1103/PhysRevA.110.023714

I. INTRODUCTION

Quantum frequency combs (QFCs) allow a large amount of quantum information encoded in a single spatial mode, facilitating an exponential acceleration in quantum information processing [1]. The capability of generating broadband quantum frequency combs stands at the forefront of quantum technology advancements [1–8]. In recent years, researchers have successfully demonstrated QFCs that enable the generation of both high-dimensional [5,9] and multiphoton entangled states [1,6]. More complex quantum states can thus be generated employing QFCs, such as cluster states, graph states, and squeezed optical combs [10–15]. Thanks to the compact, cost-efficient, and stable generation of nonclassical optical states, microcavities are inherently suitable for generating QFCs [5–9,12,14–25], holding great potential for enhancing quantum computing [1,4,25–27] and quantum communication systems [3,25,28,29].

Despite the superiority, microcavities face challenges related to waveguide dispersion, which can alter the resonance frequencies from their original positions and disrupt the essential phase-matching condition, limiting the bandwidth of spontaneous nonlinear processes and thus the dimension of QFCs [16–20]. One way to address this issue is to fine-tune the cross-section dimensions to reach near-zero anomalous dispersion. A variety of broadband QFCs have been generated in this way [30–32]. Notably, through dispersion engineering, there is potential to generate entangled photons across an octave-spanning frequency range. This technology facilitates the establishment of entanglement between bit pairs spanning both visible and telecommunications light wavelengths [33]. However, imperfections in the manufacturing process may compromise device robustness. Alternatively, phase-matching conditions can be relaxed by broadening the resonance linewidths of microcavities, which has been adopted to demonstrate an expansion of QFCs [18]. Nonetheless, the resonance broadening over the entire spectrum may degrade the nonlinear efficiency significantly and thus decrease the photon-pair generation rate (PGR) [34,35].

Recently, the manipulation of microcavity resonance peaks via parity-time ($\mathcal{PT}$) symmetry has emerged as an effective way to alter the intracavity nonlinear interactions, enabling unique photonic devices with improved performance and expanded capabilities for integrated photonics [36–41]. In this work, we develop an alternative approach to extend the spectral range of QFCs by introducing $\mathcal{PT}$ symmetry in coupled microring structures. The state evolution of $\mathcal{PT}$-symmetry coupled microcavities near the exceptional point (EP), i.e., mode splitting, merging, and broadening, leads to a rich diversity of the intracavity photon density of states (DOS) [40]. By designing the radius ratio of two coupled cavities, only the pump resonance is manipulated. Meanwhile, by employing a pulsed pump light, the effective pump frequency-matching bandwidth is found to be greatly extended on both sides of the EP. The severe phase-matching conditions of spontaneous nonlinear effects can thereby be relaxed. Consequently, substantial enhancement of the Schmidt mode number along with the dimensionality of the Hilbert space of the QFCs [32,42–44], encompassed by multiple pairs of signal and idler modes, is achieved using the proposed structure with excellent operation robustness. Furthermore, our scheme enables a

*Contact author: zhouqiang@uestc.edu.cn
†Contact author: jing_xu@hust.edu.cn
‡Contact author: xlzhang@hust.edu.cn

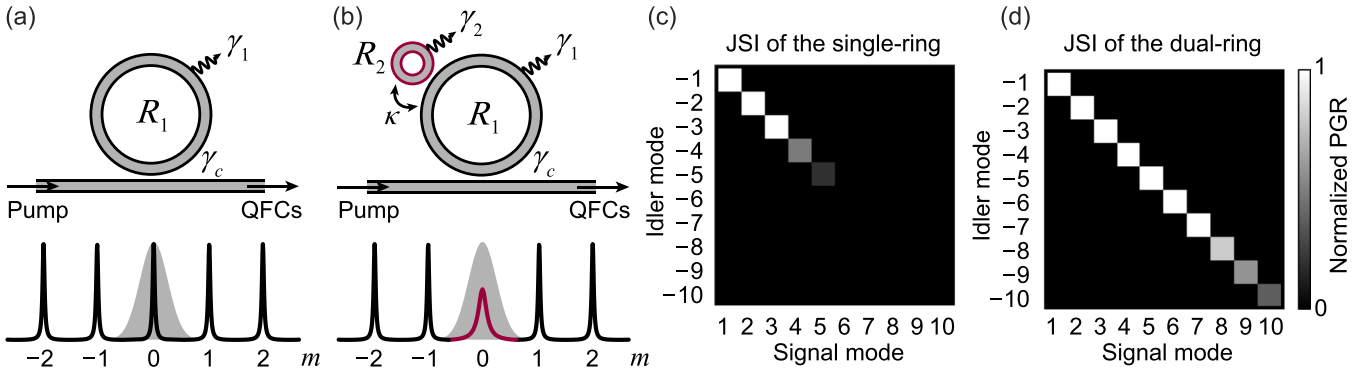

FIG. 1. Schematic diagram of (a) a conventional high-Q microresonator and (b) $\mathcal{PT}$-symmetric coupled microresonators and their corresponding photon DOS in the main ring. (a) The radius of the main ring is R_1, the intrinsic decay rate is γ_1, and the coupling coefficient between the waveguide and the ring is γ_c. (b) The auxiliary ring (red) with radius R_2 is coupled to the main ring with coupling coefficient κ. Only the pump resonance is manipulated (highlighted in red) due to the R_{FS} distinctions of the two cavities. The dashed Gaussian line shape represents the launched pulsed pump spectrum. (c), (d) are sketches of JSI among multiple frequency modes of two systems. Compared with a single-ring system, the $\mathcal{PT}$-symmetric dual-ring system presents a higher frequency dimension.

favorable balance between nonlinear efficiency and the spectrum extension of QFCs through selective manipulation of only the pump resonance [34,35]. $\mathcal{PT}$-symmetric microcavities may find important applications in enhancing the quantum information processing capacity on an integrated platform.

II. PRINCIPLE AND SYSTEM DESIGN

We begin by introducing the general structures of the proposed scheme. For comparison, a single-ring resonator system is shown in the upper panel of Fig. 1(a). A ring of radius R_1 is coupled to a bus waveguide with a coupling strength of γ_c. The intrinsic decay rate of the ring is γ_1. The corresponding intracavity DOS of photons is sketched in the lower panel of Fig. 1(a). Note that DOS is also referred to as intensity enhancement in classical photonic applications, which is defined as the ratio between intracavity field intensity and the input field intensity [39,40]. Generically, the central resonance is designated as the pump resonance (labeled as $m = 0$) to facilitate pump light, while the resonances situated symmetrically on each side of the pump are identified as the signal (labeled as $1, 2, \ldots, n$) and idler (labeled as $-1, -2, \ldots, -n$) resonances. The pulsed pump is used to cover the entire pump resonance, as shown by the shaded gray Gaussian spectrum. In a single-ring system, the quality (Q) factors of each resonance are nearly consistent. Figure 1(c) schematically illustrates the joint spectral intensity (JSI) of photon-pair generated by spontaneous four-wave mixing (SFWM) across multiple resonances under the pulsed pump, which reveals a constrained set of frequency modes because of waveguide dispersion-induced resonance variation.

Figure 1(b) shows the design of the proposed system consisting of two rings, in which the main ring—the larger one—is coupled to the auxiliary ring—the smaller one—with a radius R_2. The intrinsic decay rate of the auxiliary ring is γ_2. The coupling strength κ of two rings is variable and can be precisely controlled by adjusting the gap between the two rings. It is important to note that the ratio of the radii between the two rings R_1/R_2 is not an integer. This design introduces a large difference in the free spectral range (FSR) between the two rings [45,46]. As a result, selective coupling of only a single resonance from the auxiliary ring to the main ring can be achieved over a large spectral span. Moreover, the intrinsic loss of the auxiliary ring is set to be larger than the main one, which is accessible due to the large bending loss associated with its small radius. The coupled resonance is used as the pump resonance, which is highlighted in red in Fig. 1(b). As will be further explained below, the manipulated pump resonance near the EP features broadened linewidth or mode splitting under different system settings, providing a relaxed frequency-matching condition for SFWM. Within this system configuration, the signal and idler resonances in the main ring almost remain unaffected. The corresponding sketch of JSI is shown in Fig. 1(d), illustrating an increase in the number of frequency modes.

III. THEORY OF THE QFC GENERATION BY $\mathcal{PT}$-SYMMETRIC COUPLED MICRORINGS

Next, we elaborate on the underlying physics of relaxing the frequency-matching condition for SFWM using the mode coupling near the EP. Theoretically, the state of QFCs generated from the main ring can be derived using first-order perturbation theory under the interaction picture [32,47],

$$|\psi\rangle = \frac{\gamma W L_1}{2\pi} \iint d\omega_s d\omega_i \phi(\omega_s, \omega_i) \hat{a}_s^\dagger(\omega_s) \hat{a}_i^\dagger(\omega_i) |\mathrm{vac}\rangle, \quad (1)$$

where γ is the nonlinear coefficient, W is the energy of a single pulse, and $L_1 = 2\pi R_1$ is the circumference of the main ring. $\hat{a}_s^\dagger(\omega_s)$, $\hat{a}_i^\dagger(\omega_i)$ are the creation operators of signal and idler photons, respectively. $|\mathrm{vac}\rangle$ is the vacuum state. $\phi(\omega_s, \omega_i)$ is the joint spectral amplitude (JSA) of the two-photon state [43,44,48],

$$\phi(\omega_s, \omega_i) = \sum_{m=1} \int d\omega_p F_p(\omega_p) F_p(\omega_s + \omega_i - \omega_p) f_p(\omega_p) \times f_p(\omega_s + \omega_i - \omega_p) f_m^*(\omega_s) f_{-m}^*(\omega_i) \mathrm{sinc}\left(\frac{\Phi_m}{2}\right), \quad (2)$$

where f_m is the mth resonance, f_p is the pump resonance, and F_p is the spectrum of the launched pulsed pump. Term $\mathrm{sinc}(\Phi_m/2)$ is the waveguide dispersion-induced phase mismatch, in which $\Phi_m = \Delta\beta L_1$ is the phase mismatch accumulated over one round trip of the ring. $\Delta\beta$ is the mismatch of the propagation constants of four involving photons. Note that the square of the modulus of the JSA, $|\phi(\omega_s, \omega_i)|^2$, is commonly known as JSI [42,48], which gives the two-dimensional probability distribution of photons associated with signal and idler frequencies. Then the cavity resonances in the single-ring case shown in Fig. 1(a) can be modeled as Lorentzian line shapes [39,47],

$$f_m(\omega) = \sqrt{R_{\mathrm{FS}}}\frac{\sqrt{2\gamma_{c,m}}}{(\omega-\omega_m)-i\gamma_{\mathrm{tot},m}}, \tag{3}$$

where ω_m is the central frequency of the mth resonance, and $\gamma_{\mathrm{tot},m} = \gamma_{1,m} + \gamma_{c,m}$ is the total decay rate of the mth resonance containing the intrinsic energy decay rate $\gamma_{1,m}$ and the coupling-induced energy decay rate $\gamma_{c,m}$. R_{FS} is the FSR of the main ring. The full width at half maximum (FWHM) of resonance $\Delta\omega_m$ satisfies $\Delta\omega_m = 2\gamma_{\mathrm{tot},m}$. The Q factor of the resonance can be simply associated with the total decay rate, yielding $Q_m = \omega_m/2\gamma_{\mathrm{tot},m}$. Accordingly, the DOS of photons within the microcavity can be expressed as $|f_m(\omega)|^2$.

Regarding the pump resonance in the dual-ring system shown in Fig. 1(b), consider the operator vector $\hat{A}^\dagger = (\hat{A}_1^\dagger\ \hat{A}_2^\dagger)^T$ (where $\hat{A}_1^\dagger$, $\hat{A}_2^\dagger$ are the pump light generation operators in the main ring and the auxiliary ring, respectively). According to coupled mode theory (CMT), $\hat{A}^\dagger$ obeys the equation of motion $id\hat{A}^\dagger/dt = \hat{H}\hat{A}^\dagger - i\sqrt{\gamma_c}(\hat{A}_{\mathrm{in}}^\dagger\ 0)^T$, where the non-Hermitian Hamiltonian $\hat{H}$ is [39,40,46]

$$\hat{H} = \begin{bmatrix} \omega_0 - i(\gamma_1+\gamma_c) & \kappa \\ \kappa & \omega_0 - i\gamma_2 \end{bmatrix}. \tag{4}$$

Here, ω_0 is the central frequency of pump resonance (assuming the two rings are aligned at ω_0); $\hat{A}_{\mathrm{in}}^\dagger$ is the generation operator of the input pump light. The coupled supermodes in the $\mathcal{PT}$-symmetric system can be characterized by the complex eigenfrequencies of the Hamiltonian, calculated as

$$\omega_\pm = \left[\omega_0 - \frac{i}{2}(\gamma_1+\gamma_c+\gamma_2)\right] \pm \frac{1}{2}\sqrt{4\kappa^2 - (\gamma_1+\gamma_c-\gamma_2)^2}. \tag{5}$$

The EP of the system is at $\kappa = |\gamma_1 + \gamma_c - \gamma_2|/2$. Furthermore, for the dual-ring system, the pump resonance $f_p(\omega)$ in the main ring can be derived as

$$f_p(\omega) = \sqrt{R_{\mathrm{FS}}}\frac{\sqrt{2\gamma_c}(\omega-\omega_0-i\gamma_2)}{(\omega-\omega_+)(\omega-\omega_-)}. \tag{6}$$

According to Eqs. (5) and (6), we can regulate the shape of the pump resonance in a $\mathcal{PT}$-symmetric system by setting proper parameters, especially by tuning the coupling strength κ. For other resonances that are not coupled with the auxiliary ring, $f_m(\omega)$ can be used, as given by Eq. (3).

Figure 2(a) plots the real parts $\mathrm{Re}(\omega_\pm - \omega_0)$ (the resonant frequency deviations from ω_0) and imaginary parts $\mathrm{Im}(\omega_\pm)$ (the decay rates of $\omega_\pm$) of the supermodes with respect to the coupling strength κ, using Eq. (5). Without loss of generality, we use widely reported device parameters based on the silicon nitride-on-insulator (SNOI) platform [7,9,14,16,20,32,33]. Parameter settings are $R_1 = 115$ μm, $R_2 = 7.7$ μm, $\gamma_1 = 360$ MHz, $\gamma_c = 270$ MHz, and $\gamma_2 = 7.2$ GHz. The radius of the main ring is chosen to align with the WDM grids, with the FSR of the main ring close to 200 GHz under the condition that the group index of the silicon nitride waveguide is $n_p = 2.1$. In Fig. 2(a), the vertical distance between the two gray dashed lines encircling the eigenfrequencies on the $\mathrm{Re}(\omega_\pm - \omega_0)$ map are the linewidths of the supermodes [39]. Position (i) represents $\kappa = 0$, where the auxiliary ring is decoupled from the main ring, which means that the system is equivalent to a single-ring system shown in Fig. 1(a). The DOS of the coupled resonance ω_+ is correspondingly drawn in Fig. 2(b)(i). When the system operates in the $\mathcal{PT}$-symmetry broken regime [also known as the split-dissipation regime, position (ii), $\kappa = 1.7$ GHz], the real parts of the supermodes degenerate. The supermode

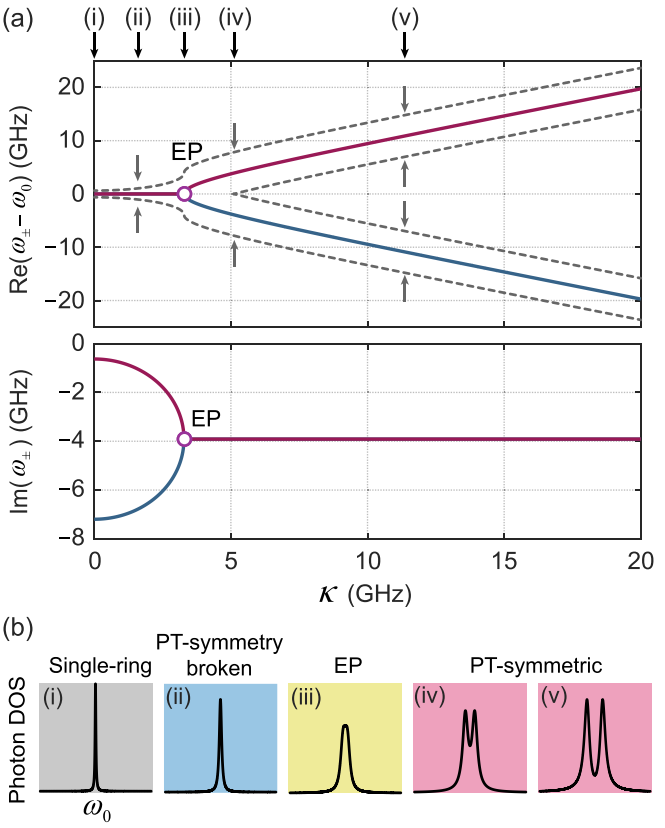

FIG. 2. Illustration of the pump resonance evolution within the $\mathcal{PT}$-symmetric system. (a) System eigenfrequency evolution varying coupling strength κ. The real parts and imaginary parts of the supermodes correspond to the resonant frequencies and decay rates, respectively. The EP satisfies $\kappa = |\gamma_1 + \gamma_c - \gamma_2|/2$. The gray dashed lines on the $\mathrm{Re}(\omega_\pm - \omega_0)$ map represent the linewidths of the supermodes. (i)–(v) are five typical system states. (i) The single-ring system, $\kappa = 0$; (ii) the $\mathcal{PT}$-symmetry broken regime, $\kappa = 1.7$ GHz; (iii) the EP, $\kappa = 3.3$ GHz; (iv) the $\mathcal{PT}$-symmetric regime, $\kappa = 5.1$ GHz, where the synthetic resonance features mode splitting and the interband ripple is less than 3 dB; (v) the $\mathcal{PT}$-symmetric regime, $\kappa = 11.7$ GHz, where the two supermodes are completely split. (b) Sketches of corresponding photon DOS within the main ring.

with less loss is characterized by a modestly broadened profile with a FWHM of $2\mathrm{Im}(\omega_+)$, as shown in Fig. 2(b)(ii). As the coupling strength κ increases, the system transitions across the EP from the $\mathcal{PT}$-symmetry broken regime into the regime where $\mathcal{PT}$ symmetry is restored. At the EP [at position (iii) the purple circle, $\kappa = 3.3$ GHz], the resonance undergoes significant broadening without mode splitting. In the $\mathcal{PT}$-symmetric regime [also known as the split-frequency regime, positions (iv) and (v), $\kappa = 5.1$ and 11.7 GHz, respectively], the two supermodes bifurcate (mode splitting) but feature the same linewidth. Although the real parts of the eigenfrequencies of the two supermodes bifurcate, the two supermodes may not separate entirely in the transmission spectrum, as depicted in the regime between Figs. 2(a)(iii) and 2(a)(iv). Here the pump resonance is highly suitable for accommodating a broadband pulsed light, with a synthesized linewidth estimated by $\mathrm{Re}(\omega_+) - \mathrm{Re}(\omega_-) + 2\mathrm{Im}(\omega_+)$ [39]. In addition, the frequency-matching range counterintuitively becomes larger in certain regimes even after two supermodes are severely split, i.e., between regimes shown by cases (iv) and (v), a phenomenon that will be explained in the following.

IV. RELAXING THE FREQUENCY-MATCHING CONDITION AND EXTENDING THE DIMENSION OF QFCs

To understand how dispersion constrains the dimension of QFCs and how the effective pump bandwidth influences the SFWM process, we analyze the JSA of two-photon QFCs. Consider the joint integral term $O(\omega_s + \omega_i) = \int d\omega_p F_p(\omega_p) F_p(\omega_s + \omega_i - \omega_p) f_p(\omega_p) f_p(\omega_s + \omega_i - \omega_p)$ extracted from Eq. (2). Physically, the FWHM of $O(\omega_s + \omega_i)$ gives the frequency-matching regions of the pump light on the JSA map [49], which is defined here as the effective pump bandwidth B_{eff}. When the bandwidth of the injected pulsed pump light, $F_p(\omega_p)$, significantly exceeds that of the resonance linewidth, B_{eff} is predominantly defined by the term $\int d\omega_p f_p(\omega_p) f_p(\omega_s + \omega_i - \omega_p)$. It is noteworthy that this term adopts a self-convolution form: $\int dy\ \mathcal{F}(y)\mathcal{F}(x-y)$, in which $x = \omega_s + \omega_i$ is the sum frequency of signal and idler lights, and $y = \omega_p$ is the pump light frequency.

Figure 3(a) maps the integral term $|O|$ with respect to the coupling strength κ. Figure 3(b) plots normalized $|O|$ with respect to frequency detuning $(\omega_s + \omega_i - 2\omega_0)$ at five typical parameters (same as in Fig. 2). From (i) to (iii), B_{eff} equals 7.05, 11.36, and 22.39 GHz, respectively. It is easy to find that B_{eff} increases as κ increases, as the system evolves from the $\mathcal{PT}$-symmetry broken regime to the EP, since the linewidth of the pump resonance is proportional to κ [see Fig. 2(a)]. In the $\mathcal{PT}$-symmetric regime, as shown in cases (iv) and (v), the self-convolution operation can, to a certain extent, compensate for the mode splitting, thereby further increasing the effective pump bandwidth. At (iv) and (v), $B_{\mathrm{eff}} = 43.81$ and 66.49 GHz, respectively. Figure 3(c) explains the self-convolution of split pump resonances. In the convolution profile, each point is determined by the overlapping area of pump resonances. This phenomenon persists until the two supermodes are completely separated [$\kappa > 15$ GHz, as can be seen in Fig. 3(a)].

Figures 4(a)–4(c) briefly sketch the JSA maps covering four resonance pairs. On this map, the diagonal line signifies

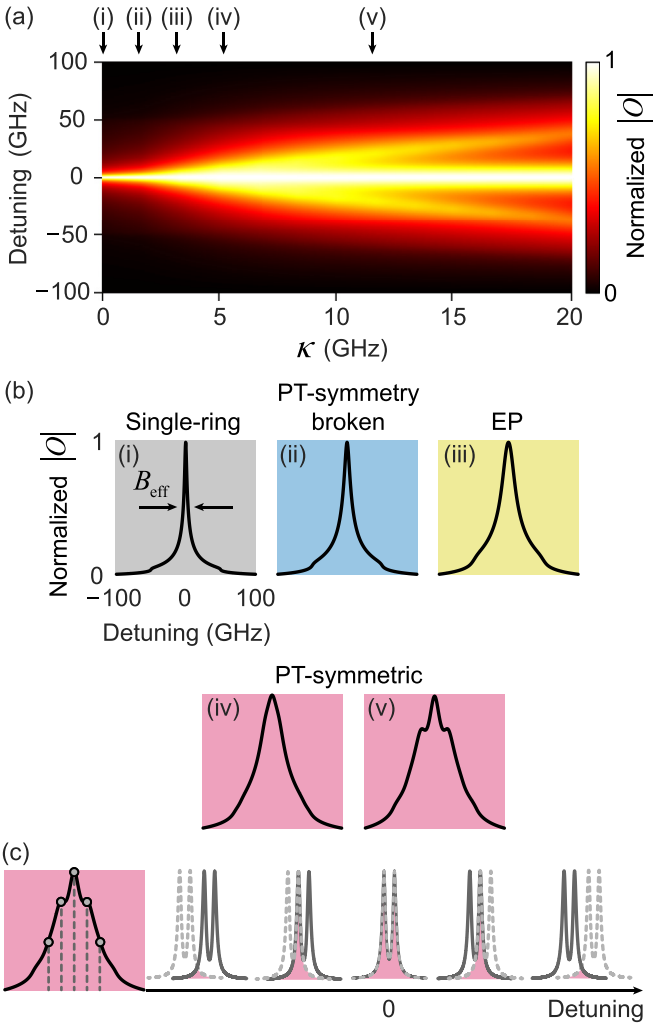

FIG. 3. Illustration of the effective pump bandwidth and frequency-matching region. (a) Effective pump bandwidth B_{eff} variations with respect to coupling strength κ. (i)–(v) are five typical parameters corresponding to Fig. 2. (b) Normalized integral term $|O|$ at different system states and the definition of B_{eff}. (c) Schematic diagram of self-convolution of split pump resonances in the $\mathcal{PT}$-symmetric regime.

the condition for frequency matching, $\omega_s + \omega_i = 2\omega_0$. The discrete diamond islands represent the combined location formed by signal and idler resonance pairs (as plotted on the coordinate axis), i.e., $f_m^*(\omega_s) f_{-m}^*(\omega_i)$ [50,51]. A uniform gray grid is superimposed on the background to illustrate the waveguide dispersion-induced mismatch in the resonant frequencies. The deviation of the center of $f_m^*(\omega_s) f_{-m}^*(\omega_i)$ from the diagonal line on the JSA map gives the extent of resonance frequency deviation from the zero-dispersion position. Such deviation can be approximated by $\sqrt{2} D_2 m^2/2$, where D_2 is extracted from the Taylor series at the pump frequency $\omega_m = \omega_0 + mD_1 + (1/2)D_2 m^2$ (higher orders are omitted) [18,46]. Here, $D_1/2\pi = R_{\mathrm{FS}} = 200$ GHz, and $D_2 = -(c/n_0)\beta_2 D_1^2 = 12$ MHz with the anomalous group velocity dispersion $\beta_2 = -50$ ps^2/km. c is the light velocity in the vacuum and $n_0 = 1.92$ is the effective refractive index. Next, B_{eff}'s are marked by the shaded areas

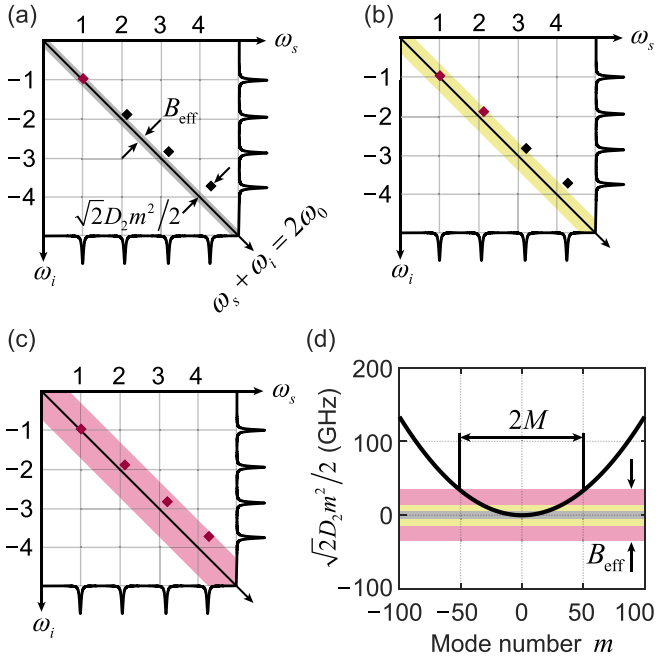

FIG. 4. Schematic diagram explaining the broadening of the effective pump bandwidth for relaxing the frequency-matching condition. (a)–(c) are brief sketches of JSA composition showing the extended QFC dimension. (d) Local dispersion-induced resonances deviation $\sqrt{2}D_2m^2/2$ with respect to the mode number on the JSA map, and the range of B_{eff}. The shaded gray, yellow, and red areas represent $B_{\text{eff}} = 7.05$, 22.39, and 66.49 GHz, respectively, corresponding to cases (i), (iii), and (v) in Figs. 2 and 3.

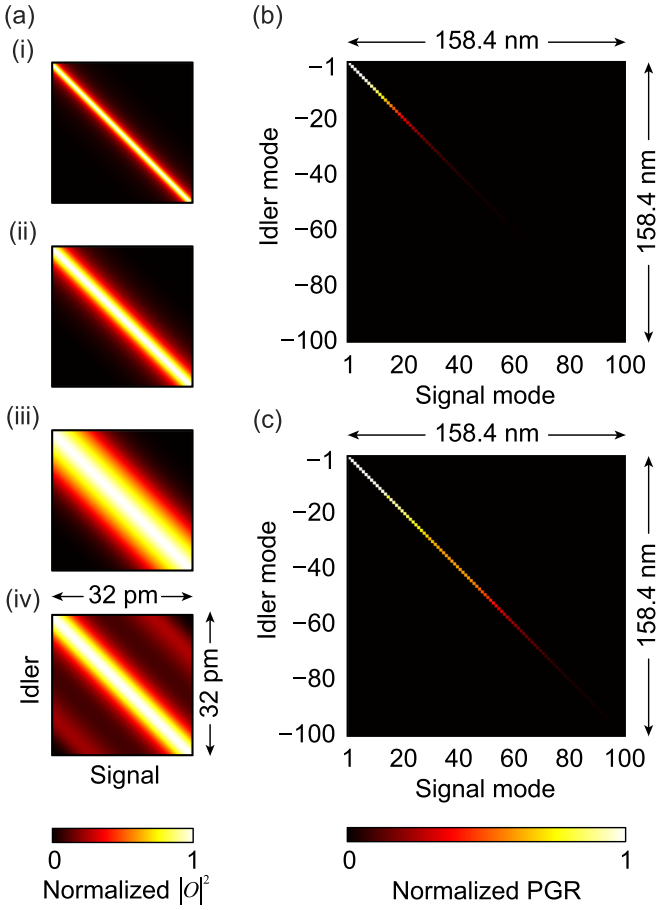

FIG. 5. Effective pump frequency-matching ranges and the simulated JSI distribution among 99 pairs of modes without and with resonance manipulation. (a) Normalized pump frequency-matching regions within the first pair of signal and idler mode $(1, -1)$ at different system settings ($B_{\text{eff}} = 7.05$, 11.36, 22.39, and 66.49 GHz). (b) The JSIs ranging across 99 pairs of modes extracted from a single-ring system. The Schmidt number is 17.87. (c) The JSI from the pump resonance manipulated dual-ring system. The coupling strength is $\kappa = 11.7$ GHz in the $\mathcal{PT}$-symmetric regime. The Schmidt number is 46.08. Note that in (b), (c), the PGRs are normalized to the first pair of mode $(1, -1)$ of each system.

along with the diagonal line. When the islands formed by signal and idler resonances are covered by the effective frequency-matching region, i.e., $B_{\text{eff}}/2 > \sqrt{2}D_2m^2/2$, the photon pairs can be created, as the islands highlighted in red in Figs. 4(a)–4(c) [the pump frequency-matching regions correspond to Figs. 3(b)(i), 3(b)(iii), and 3(b)(v), indicated by the same colors]. Therefore, the maximum mode number of QFCs, M, dictated by the effective pump bandwidth B_{eff} and the dispersion D_2 can be estimated by

$$M = \sqrt{\frac{B_{\text{eff}}}{\sqrt{2}D_2}}. \tag{7}$$

The critical impact of the effective pump bandwidth and local dispersion on the maximum mode number is further visualized in Fig. 4(d), evaluated across 99 mode pairs. The local dispersion is shown by the black line and B_{eff} is shown by the shaded areas. It is clear that by broadening the effective pump bandwidth with the assistance of a pulsed pump, the frequency-matching range can be significantly extended to resist the impact of dispersion; i.e., M increases as B_{eff} expands. Note that the phase-mismatch term $\text{sinc}(\Phi_m/2)$ in Eq. (2) also affects the bandwidth and dimension of QFCs. However, the impact of this term is trivial compared to that introduced by the frequency mismatch of resonances, especially in a ring with a small radius [18,32]. In our model, the influence of this term only becomes noticeable when m exceeds 100.

Figure 5(a) gives the effective pump frequency-matching regions on the JSI map, i.e., $|O|^2$, within the first pair of modes $(m, -m) = (1, -1)$, using real system parameters. Figure 5(a)(i) is a single-ring case ($\kappa = 0$). Figures 5(a)(ii)–5(a)(iv) are the manipulated pump resonance cases, where the state of the coupled dual-ring system is operated in the $\mathcal{PT}$-symmetry broken regime ($\kappa = 1.7$ GHz), at the EP ($\kappa = 3.3$ GHz), and in the $\mathcal{PT}$-symmetric regime ($\kappa = 11.7$ GHz), respectively. The signal and idler axes are converted into wavelength. The system operated at the EP exhibits a broader frequency-matching range than the single-ring case. In addition, the effective pump matching bandwidth is further extended in the $\mathcal{PT}$-symmetric regime thanks to the mode splitting.

Next, the JSIs across 99 pairs of modes (spanning a spectral range of approximately 158.4 nm) are numerically simulated, as drawn in Figs. 5(b) and 5(c). The PGRs are calculated

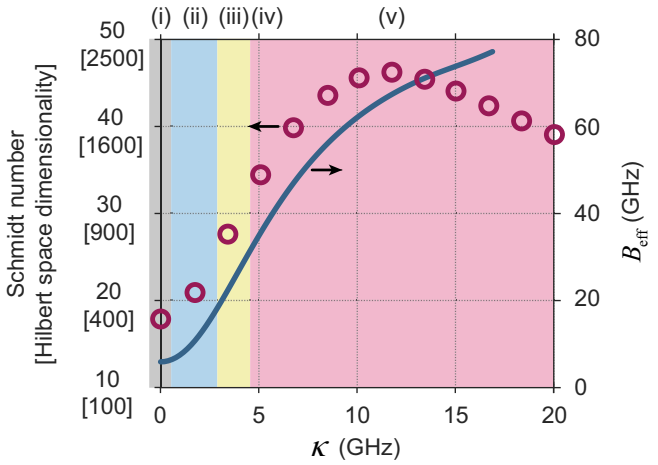

FIG. 6. Schmidt number, Hilbert space dimensionality of the QFCs, and the trend of effective pump bandwidth changes with respect to the coupling strength κ. The red circles and blue lines are the Schmidt numbers (Hilbert space dimensionality) of real systems and the corresponding effective pump bandwidth. respectively. The colors of the background correspond to Figs. 2(b) and 3(b). The maximum is reached at $\kappa = 11.7$ GHz, where mode splitting occurs within the $\mathcal{PT}$-symmetric regime. This indicates that appropriate mode splitting can further enhance the effective pump bandwidth. (i)–(v) correspond to the same region in Figs. 2–4.

by $\langle\psi|\psi\rangle$ and are normalized to the first pair of modes $(m, -m) = (1, -1)$ of each system. The Schmidt mode numbers K are determined through the Schmidt decomposition of the JSIs [18,42–44,48,51]. Figure 5(b) gives the JSI in a single-ring system [using Eq. (2)]. The Schmidt number is $K = 17.87$ and the corresponding Hilbert space dimensionality is $K \times K = 319$. The maximum mode number M predicted by Eq. (7) is $M = 20.2$ (close to the K). Using a significantly broadened effective pump bandwidth device [Fig. 5(a)(iv)], the calculated Schmidt number is up to $K = 46.08$, and the Hilbert space dimensionality is boosted to 2119, as shown in Fig. 5(c). The predicted mode number is $M = 50.6$ in this case. The Schmidt number K proportionally rises with $\sqrt{B_{\text{eff}}}$, in accordance with the maximum mode number M predicted by Eq. (7). Note that the dimensionality of the corresponding Hilbert space scales with B_{eff}.

Finally, κ is varied to explore the impact of the coupling strength between two cavities on the evolution of the dimensionality of the Hilbert space, as depicted by red circles in Fig. 6. The background colors correspond to the same regions (i)–(v) as those identified in Figs. 2 and 3. In the designed $\mathcal{PT}$-symmetric dual-ring system, as κ increases, the dimension of the QFCs continues to increase until $\kappa = 11.7$ GHz. Correspondingly, the effective pump bandwidth B_{eff} calculated by Eq. (7) is represented by the blue line, which shows a consistent trend with the dimension increase of the QFCs. When κ exceeds 11.7 GHz, the dimension begins to decline even though the effective pump bandwidth continues to increase. This is due to the strong mode splitting within the range of the effective pump frequency-matching [see bifurcations in Fig. 3(a)] region. When κ exceeds 17.1 GHz, the definition of B_{eff} becomes invalid due to the intraband ripples larger than 3 dB. Good agreement has been found between the Schmidt number K and B_{eff} over a wide coupling regime, indicating that Eq. (7) offers a convenient and rapid method for estimating the Schmidt number of QFCs.

It is worth noting that the high-Q cavities feature narrow linewidths, thus suffering from more strict frequency-matching conditions since the dimension of QFCs in high-Q cavities is limited not only by the pump resonance but also the linewidths of signal and idler resonances. This has been discussed thoroughly in Ref. [18], where the authors exploited a reconfigurable resonator to lower the Q of the cavity by overcoupling the resonator to the bus waveguide. However, the additional losses introduced to all the resonances can severely harm the SFWM efficiency [34,35]. Our scheme decouples the linewidths relation of pump and signal and idler resonances, relieving the reduction of efficiency by only manipulating the pump resonance. Using a pulsed pump, we provide a more effective way to deal with the trade-off between the SFWM efficiency and the spectral range of the QFCs, particularly in high-Q cavities.

V. CONCLUSION

In conclusion, we have analyzed the decisive roles of effective pump bandwidth and dispersion on the dimensions of QFCs, and proposed the expansion of the dimensions of QFCs through the manipulation of pump resonance utilizing $\mathcal{PT}$ symmetry. By designing a dual-ring coupled system and by controlling the system parameters, the pump resonance can exhibit broadening or mode splitting. We have shown that $\mathcal{PT}$ symmetry facilitates powerful spectrum manipulation, effectively broadening the pump frequency-matching range on both sides of the EP with the help of a pulsed pump, leading to the generation of higher-dimensional quantum microcombs. QFCs spanning over a 200 nm spectral range have been predicted. The corresponding Schmidt number of QFCs is increased from 17.87 to 46.08, and the Hilbert space dimensionality is boosted from 319 to 2119. We anticipate that broadband QFC generation based on the spectral manipulation of microcavities achieved through $\mathcal{PT}$ symmetry can find applications in a wider range of fields in integrated quantum optics; for instance, it may be used for the high-dimensional entanglement state [1,4,5,9], and complex quantum state generation [10–15].

The data underlying the results presented in the study are available upon reasonable request from the corresponding author(s).

ACKNOWLEDGMENTS

This work is supported by the National Natural Science Foundation of China (NSFC) (Grant No. 62275087); Sichuan Science and Technology Program (Grants No. 2022YFSY0061 and No. 2021YFSY0065); The Knowledge Innovation Program of Wuhan-Shuguang Project (Grant No. 2022010801010082); and Fundamental Research Funds for the Central Universities, HUST (Grant No. 5003182133).

The authors declare no conflicts of interest.

[1] M. Kues, C. Reimer, J. M. Lukens, W. J. Munro, A. M. Weiner, D. J. Moss, and R. Morandotti, Quantum optical microcombs, Nat. Photon. **13**, 170 (2019).

[2] M. A. Guidry, D. M. Lukin, K. Y. Yang, R. Trivedi, and J. Vučković, Quantum optics of soliton microcombs, Nat. Photon. **16**, 52 (2022).

[3] H.-H. Lu, M. Liscidini, A. L. Gaeta, A. M. Weiner, and J. M. Lukens, Frequency-bin photonic quantum information, Optica **10**, 1655 (2023).

[4] M. Erhard, M. Krenn, and A. Zeilinger, Advances in high-dimensional quantum entanglement, Nat. Rev. Phys. **2**, 365 (2020).

[5] M. Kues, C. Reimer, P. Roztocki, L. R. Cortés, S. Sciara, B. Wetzel, Y. Zhang, A. Cino, S. T. Chu, B. E. Little, D. J. Moss, L. Caspani, J. Azaña, and R. Morandotti, On-chip generation of high-dimensional entangled quantum states and their coherent control, Nature (London) **546**, 622 (2017).

[6] C. Reimer, M. Kues, P. Roztocki, B. Wetzel, F. Grazioso, B. E. Little, S. T. Chu, T. Johnston, Y. Bromberg, L. Caspani, D. J. Moss, and R. Morandotti, Generation of multiphoton entangled quantum states by means of integrated frequency combs, Science **351**, 1176 (2016).

[7] C. Reimer, L. Caspani, M. Clerici, M. Ferrera, M. Kues, M. Peccianti, A. Pasquazi, L. Razzari, B. E. Little, S. T. Chu, D. J. Moss, and R. Morandotti, Integrated frequency comb source of heralded single photons, Opt. Express **22**, 6535 (2014).

[8] J. Chen, Z. H. Levine, J. Fan, and A. L. Migdall, Frequency-bin entangled comb of photon pairs from a silicon-on-insulator micro-resonator, Opt. Express **19**, 1470 (2011).

[9] P. Imany, J. A. Jaramillo-Villegas, O. D. Odele, K. Han, D. E. Leaird, J. M. Lukens, P. Lougovski, M. Qi, and A. M. Weiner, 50-GHz-spaced comb of high-dimensional frequency-bin entangled photons from an on-chip silicon nitride microresonator, Opt. Express **26**, 1825 (2018).

[10] Z. Xie, T. Zhong, S. Shrestha, X. Xu, J. Liang, Y.-X. Gong, J. C. Bienfang, A. Restelli, J. H. Shapiro, F. N. C. Wong, and C. W. Wong, Harnessing high-dimensional hyperentanglement through a biphoton frequency comb, Nat. Photon. **9**, 536 (2015).

[11] Y. Cai, J. Roslund, G. Ferrini, F. Arzani, X. Xu, C. Fabre, and N. Treps, Multimode entanglement in reconfigurable graph states using optical frequency combs, Nat. Commun. **8**, 15645 (2017).

[12] J. A. Jaramillo-Villegas, P. Imany, O. D. Odele, D. E. Leaird, Z.-Y. Ou, M. Qi, and A. M. Weiner, Persistent energy–time entanglement covering multiple resonances of an on-chip biphoton frequency comb, Optica **4**, 655 (2017).

[13] M. Pysher, Y. Miwa, R. Shahrokhshahi, R. Bloomer, and O. Pfister, Parallel generation of quadripartite cluster entanglement in the optical frequency comb, Phys. Rev. Lett. **107**, 030505 (2011).

[14] M. Jahanbozorgi, Z. Yang, S. Sun, H. Chen, R. Liu, B. Wang, and X. Yi, Generation of squeezed quantum microcombs with silicon nitride integrated photonic circuits, Optica **10**, 1100 (2023).

[15] Z. Yang, M. Jahanbozorgi, D. Jeong, S. Sun, O. Pfister, H. Lee, and X. Yi, A squeezed quantum microcomb on a chip, Nat. Commun. **12**, 4781 (2021).

[16] Y. Fan, C. Lyu, C. Yuan, G. Deng, Z. Zhou, Y. Geng, H. Song, Y. Wang, Y. Zhang, R. Jin, H. Zhou, L. X. You, Z. Wang, G. Guo, and Q. Zhou, Multi-wavelength quantum light sources on silicon nitride micro-ring chip, Laser Photon. Rev. **17**, 2300172 (2023).

[17] Z. Jiang, Y. Chen, C. Jiang, and G. He, Generation of quantum optical frequency combs in topological resonators, Adv. Quantum Technol. **7**, 2300354 (2024).

[18] C. Wu, Q. Zheng, Y. Liu, Y. Wang, J. Ding, P. Zhu, S. Xue, M. Yu, W. Luo, K. Zhang, A. Huang, M. Deng, J. Wu, and P. Xu, Boosting the dimensionality of frequency entanglement using a reconfigurable microring resonator, Sci. China: Phys. Mech. Astron. **66**, 250312 (2023).

[19] Q. Zheng, J. Liu, C. Wu, S. Xue, P. Zhu, Y. Wang, X. Yu, M. Yu, M. Deng, J. Wu, and P. Xu, Bright 547-dimensional Hilbert-space entangled resource in 28-pair modes biphoton frequency comb from a reconfigurable silicon microring resonator, Chin. Phys. B **31**, 024206 (2022).

[20] W. Wen, W. Yan, C. Lu, L. Lu, X. Wu, Y. Lu, S. Zhu, and X.-S. Ma, Polarization-entangled quantum frequency comb from a silicon nitride microring resonator, Phys. Rev. Appl. **20**, 064032 (2023).

[21] F. Mazeas, M. Traetta, M. Bentivegna, F. Kaiser, D. Aktas, W. Zhang, C. A. Ramos, L. A. Ngah, T. Lunghi, É. Picholle, N. Belabas-Plougonven, X. Le Roux, É. Cassan, D. Marris-Morini, L. Vivien, G. Sauder, L. Labonté, and S. Tanzilli, High-quality photonic entanglement for wavelength-multiplexed quantum communication based on a silicon chip, Opt. Express **24**, 28731 (2016).

[22] M. Fujiwara, R. Wakabayashi, M. Sasaki, and M. Takeoka, Wavelength division multiplexed and double-port pumped time-bin entangled photon pair generation using Si ring resonator, Opt. Express **25**, 3445 (2017).

[23] B. Xu, L. Chen, J. Lin, L. Feng, R. Niu, Z. Zhou, R. Gao, C. Dong, G. Guo, Q. Gong, Y. Cheng, Y. Xiao, and X. Ren, Spectrally multiplexed and bright entangled photon pairs in a lithium niobate microresonator, Sci. China: Phys. Mech. Astron. **66**, 294262 (2022).

[24] H. Zeng *et al.*, Quantum light generation based on GaN microring toward fully on-chip source, Phys. Rev. Lett. **132**, 133603 (2024).

[25] W. Luo, L. Cao, Y. Shi, L. Wan, H. Zhang, S. Li, G. Chen, Y. Li, S. Li, Y. Wang, S. Sun, M. F. Karim, H. Cai, L. C. Kwek, and A. Q. Liu, Recent progress in quantum photonic chips for quantum communication and internet, Light: Sci. Appl. **12**, 175 (2023).

[26] C. Reimer, S. Sciara, P. Roztocki, M. Islam, L. Romero Cortés, Y. Zhang, B. Fischer, S. Loranger, R. Kashyap, A. Cino, S. T. Chu, B. E. Little, D. J. Moss, L. Caspani, W. J. Munro, J. Azaña, M. Kues, and R. Morandotti, High-dimensional one-way quantum processing implemented on d-level cluster states, Nat. Phys. **15**, 148 (2019).

[27] P. Imany, J. A. Jaramillo-Villegas, M. S. Alshaykh, J. M. Lukens, O. D. Odele, A. J. Moore, D. E. Leaird, M. Qi, and A. M. Weiner, High-dimensional optical quantum logic in large operational spaces, npj Quantum Inf. **5**, 59 (2019).

[28] S. Wengerowsky, S. K. Joshi, F. Steinlechner, H. Hübel, and R. Ursin, An entanglement-based wavelength-multiplexed quantum communication network, Nature (London) **546**, 225 (2018).

[29] W. Wen, Z. Chen, L. Lu, W. Yan, W. Xue, P. Zhang, Y. Lu, S. Zhu, and X.-S. Ma, Realizing an entanglement-based multiuser

quantum network with integrated photonics, Phys. Rev. Appl. **18**, 024059 (2022).

[30] K. Sugiura, Z. Yin, R. Okamoto, L. Zhang, L. Kang, J. Chen, P. Wu, S. T. Chu, B. E. Little, and S. Takeuchi, Broadband generation of photon-pairs from a CMOS compatible device, Appl. Phys. Lett. **116**, 224001 (2020).

[31] F. Samara, A. Martin, C. Autebert, M. Karpov, T. J. Kippenberg, H. Zbinden, and R. Thew, High-rate photon pairs and sequential time-bin entanglement with Si_3N_4 microring resonators, Opt. Express **27**, 19309 (2019).

[32] Z. Yin, K. Sugiura, H. Takashima, R. Okamoto, F. Qiu, S. Yokoyama, and S. Takeuchi, Frequency correlated photon generation at telecom band using silicon nitride ring cavities, Opt. Express **29**, 4821 (2021).

[33] X. Lu, Q. Li, D. A. Westly, G. Moille, A. Singh, V. Anant, and K. Srinivasan, Chip-integrated visible–telecom entangled photon pair source for quantum communication, Nat. Phys. **15**, 373 (2019).

[34] N. Chen, Z. Wang, J. Wu, H. Li, S. He, Z. Fan, Y. Fan, X. Zhang, Q. Zhou, and J. Xu, Pushing photon-pair generation rate in microresonators by Q factor manipulation, Opt. Lett. **48**, 5355 (2023).

[35] K. Guo, X. Shi, X. Wang, J. Yang, Y. Ding, H. Ou, and Y. Zhao, Generation rate scaling: The quality factor optimization of microring resonators for photon-pair sources, Photon. Res. **6**, 587 (2018).

[36] Ş. K. Özdemir, S. Rotter, F. Nori, and L. Yang, Parity–time symmetry and exceptional points in photonics, Nat. Mater. **18**, 783 (2019).

[37] L. Feng, R. El-Ganainy, and L. Ge, Non-Hermitian photonics based on parity–time symmetry, Nat. Photon. **11**, 752 (2017).

[38] L. Chang, X. Jiang, S. Hua, C. Yang, J. Wen, L. Jiang, G. Li, G. Wang, and M. Xiao, Parity–time symmetry and variable optical isolation in active–passive-coupled microresonators, Nat. Photon. **8**, 524 (2014).

[39] C. Kim, X. Lu, D. Kong, N. Chen, Y. Chen, L. K. Oxenløwe, K. Yvind, X. Zhang, L. Yang, M. Pu, and J. Xu, Parity-time symmetry enabled ultra-efficient nonlinear optical signal processing, eLight **4**, 6 (2024).

[40] B. Peng, Ş. K. Özdemir, F. Lei, F. Monifi, M. Gianfreda, G. L. Long, S. Fan, F. Nori, C. M. Bender, and L. Yang, Parity–time-symmetric whispering-gallery microcavities, Nat. Phys. **10**, 394 (2014).

[41] B. Peng, K. Ozdemir, S. Rotter, H. Yilmaz, M. Liertzer, F. Monifi, C. M. Bender, F. Nori, and L. Yang, Loss-induced suppression and revival of lasing, Science **346**, 328 (2014).

[42] Z. Vernon, M. Menotti, C. C. Tison, J. A. Steidle, M. L. Fanto, P. M. Thomas, S. F. Preble, A. M. Smith, P. M. Alsing, M. Liscidini, and J. E. Sipe, Truly unentangled photon pairs without spectral filtering, Opt. Lett. **42**, 3638 (2017).

[43] L. Caspani, C. Xiong, B. J. Eggleton, D. Bajoni, M. Liscidini, M. Galli, R. Morandotti, and D. J. Moss, Integrated sources of photon quantum states based on nonlinear optics, Light: Sci. Appl. **6**, e17100 (2017).

[44] S. Signorini and L. Pavesi, On-chip heralded single photon sources, AVS Quantum Sci. **2**, 041701 (2020).

[45] Ó. B. Helgason, M. Girardi, Z. Ye, F. Lei, J. Schröder, and V. Torres-Company, Surpassing the nonlinear conversion efficiency of soliton microcombs, Nat. Photon. **17**, 992 (2023).

[46] B. Zhang, N. Chen, H. Yang, Y. Chen, J. Dong, H. Zhou, X. Zhang, and J. Xu, Dispersion-suppressed mode depletion by exceptional points for on-chip nonlinear optics, Phys. Rev. Appl. **18**, 034028 (2022).

[47] C. Wu, Y. Liu, Y. Wang, J. Ding, P. Zhu, S. Xue, X. Yu, Q. Zheng, M. Yu, A. Huang, X. Fu, X. Qiang, M. Deng, J. Wu, and P. Xu, Optimization of quantum light sources and four-wave mixing based on a reconfigurable silicon ring resonator, Opt. Express **30**, 9992 (2022).

[48] K. Zielnicki, K. Garay-Palmett, D. Cruz-Delgado, H. Cruz-Ramirez, M. F. O'Boyle, B. Fang, V. O. Lorenz, A. B. U'Ren, and P. G. Kwiat, Joint spectral characterization of photon-pair sources, J. Mod. Opt. **65**, 1141 (2018).

[49] E. Ortiz-Ricardo, C. Bertoni-Ocampo, M. Maldonado-Terrón, A. Garcia Zurita, R. Ramirez-Alarcon, H. Cruz Ramirez, R. Castro-Beltrán, and A. B. U'Ren, Submegahertz spectral width photon pair source based on fused silica microspheres, Photon. Res. **9**, 2237 (2021).

[50] H. Yu, C. Yuan, R. Zhang, Z. Zhang, H. Li, Y. Wang, G. Deng, L. You, H. Song, Z. Wang, G.-C. Guo, and Q. Zhou, Spectrally multiplexed indistinguishable single-photon generation at telecom-band, Photon. Res. **10**, 1417 (2022).

[51] R. Kumar, J. R. Ong, M. Savanier, and S. Mookherjea, Controlling the spectrum of photons generated on a silicon nanophotonic chip, Nat. Commun. **5**, 5489 (2014).